ACS APPLIED MATERIALS & INTERFACES
Research Article
www.acsami.org

Enhanced Performance of Solution-Processed Organic Thin-Film Transistors with a Low-Temperature-Annealed Alumina Interlayer between the Polyimide Gate Insulator and the Semiconductor

Jun-Young Yoon, Sunho Jeong, Sun Sook Lee, Yun Ho Kim, Jae-Won Ka, Mi Hye Yi,* and Kwang-Suk Jang*

Division of Advanced Materials, Korea Research Institute of Chemical Technology, 141 Gajeong-ro, Yuseong-gu, Daejeon 305-600, Republic of Korea

Supporting Information

ABSTRACT: We studied a low-temperature-annealed sol–gel-derived alumina interlayer between the organic semiconductor and the organic gate insulator for high-performance organic thin-film transistors. The alumina interlayer was deposited on the polyimide gate insulator by a simple spin-coating and 200 °C-annealing process. The leakage current density decreased by the interlayer deposition: at 1 MV/cm, the leakage current densities of the polyimide and the alumina/polyimide gate insulators were 7.64 × 10^{-7} and 3.01 × 10^{-9} A/cm^2, respectively. For the first time, enhancement of the organic thin-film transistor performance by introduction of an inorganic interlayer between the organic semiconductor and the organic gate insulator was demonstrated: by introducing the interlayer, the field-effect mobility of the solution-processed organic thin-film transistor increased from 0.35 ± 0.15 to 1.35 ± 0.28 cm^2/V·s. Our results suggest that inorganic interlayer deposition could be a simple and efficient surface treatment of organic gate insulators for enhancing the performance of solution-processed organic thin-film transistors.

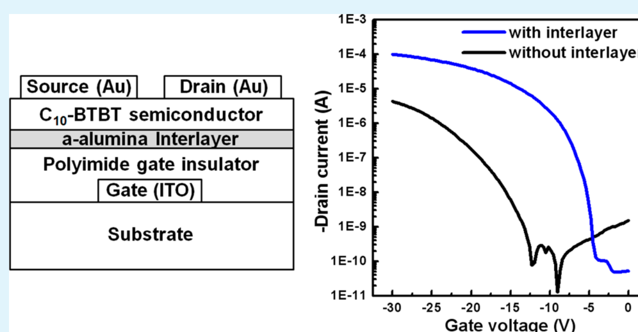

KEYWORDS: *gate insulators, solution process, spin-coating, interlayer, organic thin-film transistors*

INTRODUCTION

During the past few decades, a great deal of attention has been paid to organic thin-film transistors (OTFTs) because they are considered to be applicable to low-cost, large-area, and flexible electronics.[1−10] A variety of high-performance, solution-processable organic semiconductors (OSCs) have been developed, while research on organic gate insulators (OGIs) has been more limited. Among the various high-performance OSCs, 2,7-dialky[1]benzothieno[3,2-b][1]benzothiophenes (C_n-BTBTs) are known to be solution-processable and air-stable *p*-type OSCs.[11−18] C_n-BTBT TFTs have shown excellent TFT performance. For example, the OTFTs with C_8-BTBT, deposited on a SiO_2 gate insulator by drop-casting with a sustaining piece, exhibited mobilities of up to 6 cm^2/V·s.[16,17] The OTFTs with single-crystal C_8-BTBT, deposited on a chemical vapor deposited parylene C gate insulator by double-shot ink jet printing, showed mobilities up to 31 cm^2/V·s.[15] For the potential applications in low-cost and flexible electronics, solution-processed OGIs could be used instead of thermally grown SiO_2 or chemical vapor deposited Parylene C gate insulators. There are few reports on C_n-BTBT TFTs with solution-processed OGIs. For example, Naito et al. reported the top-gate C_8-BTBT TFT with the solution-processed fluoropolymer gate insulator.[19] In our previous study, the bottom-gate C_{10}-BTBT TFT with the solution-processed polyimide gate insulator exhibited a maximum field-effect mobility of 0.56 cm^2/V·s and threshold voltage (V_{th}) of −44.0 V.[20] C_n-BTBTs are known to be air-stable because of their low highest occupied molecular orbital (HOMO) energy level, though the huge negative shift of V_{th} is thought to be a drawback.[16−20] The performance of C_{10}-BTBT TFTs with OGIs, including the relatively low field-effect mobility and the negative shift of V_{th}, still needs to be improved for a variety of electronics applications.

To improve the OTFT performance, surface modification of gate insulators has been widely utilized. For example, OTFTs with self-assembled monolayer (SAM)-treated SiO_2 gate insulators exhibited better device performance than those with bare SiO_2 gate insulators.[21−31] It is believed that the SAM treatment results in reducing traps originating from surface hydroxyl groups of SiO_2 gate insulators and improving the crystal quality of OSC molecules. Surface properties of SiO_2 gate insulators could be modified by the SAM treatment;

Received: March 19, 2013
Accepted: May 21, 2013
Published: May 21, 2013

ACS Publications © 2013 American Chemical Society

however, surface modification of OGIs is more limited due to the lack of functional groups such as surface hydroxide.

In this paper, we report on the enhanced performance of solution-processed C_{10}-BTBT TFTs by introduction of a low-temperature-annealed sol−gel-derived amorphous alumina (a-alumnia) interlayer between the OGI and the OSC. The a-alumina thin film was solution processable at low temperatures compatible with flexible substrates.[32] We demonstrate that the inorganic interlayer deposition could be a simple and efficient OGI-surface-treatment way for enhancing the performance of solution-processed OTFTs. The a-alumina interlayer is deposited on the polyimide gate insulator using a simple spin-coating and 200 °C-annealing process. By the introduction of the a-alumina interlayer, the field-effect mobility improves from 0.18 to 1.42 $cm^2/V \cdot s$ and the turn-on voltage (V_{on}) shifts from −12.3 to −3.9 V. To the best of our knowledge, the enhancement of the OTFT performance by introduction of the inorganic interlayer between the OGI and the OSC has not been reported before. Our results prove that the surface characteristics of the underlying a-alumina interlayer facilitates the improvement of the crystal quality of OSC molecules, and the remaining nitrate in the a-alumina layer plays a critical role as an electron acceptor for approaching the turn-on voltage toward a zero bias, which maintains the acceptable electrical properties as an interlayer.

■ RESULTS AND DISCUSSION

We prepared the polyimide (KPI) precursor, the poly(amic acid) from a dianhydride monomer of 3,3′4,4′-biphenyl tetracarboxylic dianhydride (BPDA), and a diamine monomer of *p*-phenylenediamine (*p*-PDA). To decrease the imidization temperature, a base catalyst, 1,8-diazabicyclo[5.4.0]undec-7-ene (DBU), was added to the poly(amic acid) solution.[33] To obtain the polyimide gate insulator, the poly(amic acid) solution with DBU was spin-coated and annealed at 200 °C. For the deposition of the a-alumina interlayer, aluminum nitrate nonahydrate/2-butoxyethanol solution was spin-coated on the KPI gate insulator and annealed at 200 °C. The thicknesses of the KPI and the a-alumina/KPI films were controlled to be 120 and 140 nm, respectively. It is known that a-alumina thin films can be formed at low temperatures compatible with flexible substrates. In a previous study, the a-alumina thin film, solution processed at 200 °C, was successfully used as a gate insulator for inorganic TFTs.[32] Similar low-temperature approaches were reported for enhancing the performance of polymer solar cells. Amorphous ZnO interlayers, solution processed at a temperature below 200 °C, were used as an electron transport layer.[34,35] To determine the effective annealing temperature for the a-alumina interlayer, thermal gravimetric analysis (TGA) was conducted. Figures S1 and S2, Supporting Information, show the thermal behaviors of the aluminum nitrate nonahydrate precursors as a function of temperature ranging from 25 to 500 °C and as a function of annealing time at 200 °C, respectively. The weight loss at 200 °C was 76.5% (weight loss at 50 min in Figure S2, Supporting Information), which is comparable to the maximum weight loss by the thermal decomposition, 82.9% (weight loss at 450 °C in Figure S1, Supporting Information). Thus, the low-temperature annealing at 200 °C for a prolonged time is thought to be sufficient for the almost complete thermal decomposition of the precursor. To elucidate the formation of the oxide skeleton framework, even by a low-temperature process, the chemical structure of the resulting alumina layer was analyzed with X-ray photoelectron spectroscopy (XPS), as shown in Figure 1. The near-Gaussian peak at 529.5 ± 0.5 eV indicates an oxide lattice with

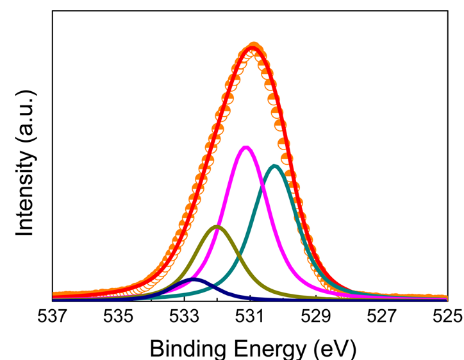

Figure 1. XPS spectrum of a-alumina interlayer on KPI film.

a chemical bond of Al−O, whereas the peak at 531 ± 0.5 eV implies an oxygen-deficient oxide lattice, i.e., an oxide lattice with an oxygen vacancy. The feature at ∼532.0 eV is assigned to the oxygen in the hydroxide due to highly electronegative hydrogen atoms. The peak for nitrate, which comes from the partially decomposed precursor, is located at ∼533 eV. It is clear that the oxide skeleton forms, even by annealing at 200 °C, with the presence of a small amount of hydroxide and nitrate. For oxide materials applicable to a gate insulator for TFTs, the hydroxide acts as a trap site for electrons, which gives rise to the electrical conduction path for the leakage current. By increasing the annealing temperature, further formation of the oxide lattice proceeds by converting the hydroxide into a metal oxide framework via a thermally enhanced condensation reaction. However, the ultrathin a-alumina layer suggested in this study is mainly composed of oxide lattices that endow reasonable insulating properties, as shown in Figure S3, Supporting Information.

The amorphous phase of a-alumina on KPI was confirmed by X-ray diffraction (XRD) analysis (Figure S4, Supporting Information). Figure 2a,b shows atomic force microscope (AFM) images of KPI and a-alumina/KPI films, respectively. Surface root-mean-square (rms) roughnesses, calculated from the AFM images (5 μm × 5 μm), of the KPI and a-alumina/KPI films were 1.02 and 0.70 nm, respectively. Both films have a smooth surface. Surface energies were calculated from contact angles of water and diiodomethane. The measured surface energies of the KPI and a-alumina/KPI films were 51.4 and 69.3 dyn/cm, respectively.

To show the effect of the interlayer deposition on the gate insulating properties, metal−insulator−metal (MIM) capacitor structures were fabricated. Figure 3a shows the frequency-dependent capacitances of the120 nm-thick KPI film and the 140 nm-thick a-alumina/KPI film. At a frequency range of 40 Hz to 10 kHz, the dielectric constants of the KPI and the a-alumina/KPI gate insulators were calculated to be in the range of 3.1−3.2 and 3.2−3.4, respectively. Figure 3b shows the electric field-dependent leakage current densities of the KPI and the a-alumina/KPI gate insulators. Interestingly, the leakage current density decreased by the deposition of the interlayer. At 1 MV/cm, the leakage current densities of the KPI and the a-alumina/KPI gate insulators were 7.64×10^{-7} and 3.01×10^{-9} A/cm^2, respectively. The deposition of the amorphous nanolayer could suppress the leakage current by termination of the grain boundaries, defects, pinholes, and

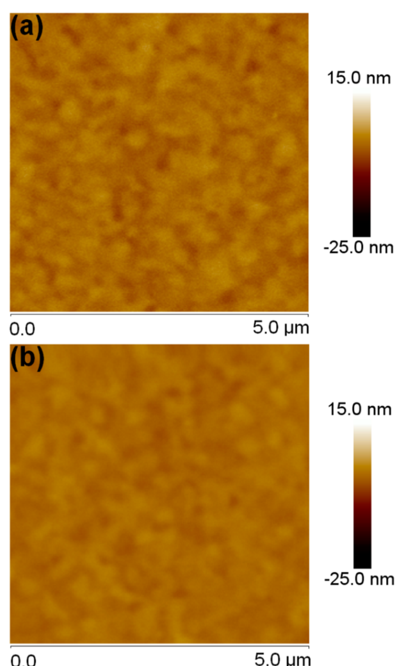

Figure 2. AFM images of (a) KPI and (b) a-alumina/KPI films.

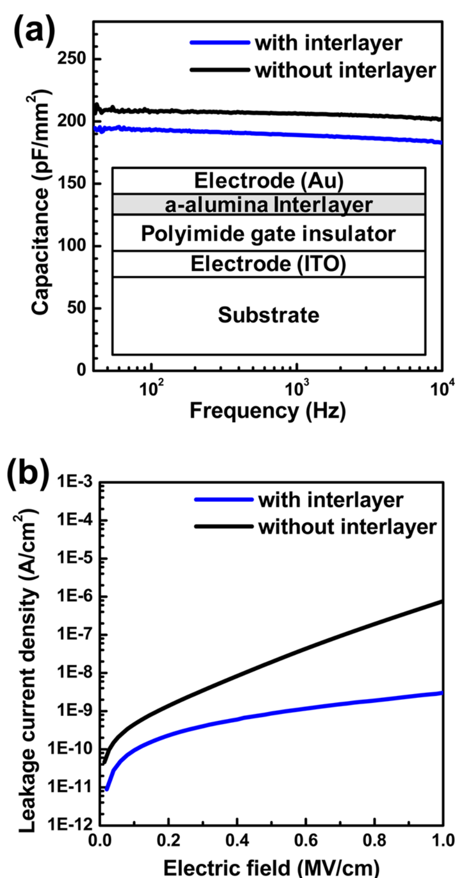

Figure 3. (a) Capacitances (as a function of frequency) and (b) leakage current densities (as a function of electric field) of KPI and a-alumina/KPI films.

clusters in the multilayer thin films.[36,37] The a-alumina-deposited KPI gate insulator had better gate insulating properties than the bare KPI gate insulator, as summarized in Table 1.

Table 1. Dielectric, Insulating, and Surface Properties of KPI and a-Alumina/KPI Films

gate insulator	dielectric constant[a]	leakage current density[b] [A/cm^2]	surface rms roughness [nm]	surface energy [dyn/cm]
KPI	3.13	7.64×10^{-7}	1.02	51.4
a-alumina/KPI	3.26	3.01×10^{-9}	0.70	69.3

[a]Measured at 10 kHz. [b]Measured at 1 MV/cm.

To investigate the effect of the a-alumina interlayer on the OTFT performance, we fabricated solution-processed C_{10}-BTBT TFTs with a bottom-gate, top-contact geometry. Among the various methods for OSC deposition, a simple spin-coating method was used in this study. In a previous study, the OTFTs with C_{10}-BTBT, deposited on the SiO_2 gate insulator by the spin-coating, had mobilities in the range of 0.28 to 0.86 cm^2/V·s.[11] The OTFT device structure used in this study is shown in Figure 4a. The a-alumina interlayer between the OGI and the OSC significantly affected the OTFT performance. Figure 4b–d shows the transfer and output characteristics of the C_{10}-BTBT TFTs with and without the a-alumina interlayer. The OTFTs showed typical *p*-type characteristics. The field-effect mobility, V_{on}, V_{th}, subthreshold slope (*S*-slope), and on/off current values are summarized in Table 2. By the introduction of the a-alumina interlayer, the field-effect mobility increased from 0.18 to 1.42 cm^2/V·s, V_{on} increased from −12.3 to −3.9 V, V_{th} increased from −18.6 to −7.0 V, and the *S*-slope decreased from 3.27 to 0.42 V/decade. To compare the device performance, we prepared 10 OTFT devices for each case. The on/off current ratios of all the OTFTs were >10^5. The average field-effect mobility, V_{th}, and *S*-slope of the C_{10}-BTBT TFTs with the a-alumina interlayer were 1.35 ± 0.27 cm^2/V·s, −6.55 ± 1.67 V, and 2.16 ± 0.77 V/decade, respectively. Those of the C_{10}-BTBT TFTs without the a-alumina interlayer were 0.35 ± 0.15 cm^2/V·s, −17.5 ± 1.28 V, and 3.45 ± 0.43 V/decade, respectively. For more comparison, the C_{10}-BTBT TFTs with the 100 nm-thick SiO_2 gate insulators were also prepared (Figure S5, Supporting Information, and Table 2). The on/off current ratios and the average field-effect mobility of the prepared devices were >10^5 and 0.39 ± 0.11 cm^2/V·s, respectively. All three types of OTFTs had a small hysteresis of less than 1 V in the transfer characteristics (Figures S5, S6, and S7, Supporting Information).

By introducing the a-alumina interlayer, the OTFT performance was greatly enhanced. The enhanced performance might be related to the C_{10}-BTBT morphology. Figure 5a,b shows AFM images of C_{10}-BTBT layers on the KPI and a-alumina/KPI films. In both images, there are two-dimensional (2D) layers and three-dimensional (3D) islands of C_{10}-BTBT crystals. The layer-plus-island formation of OSC molecules, i.e., the Stranski-Krastanov mode, occurs when the OSC's intermolecular and substrate–molecule interactions are placed in some balanced range.[23] The diameters of the 3D islands on the KPI film are much larger than those on the a-alumina/KPI film. 2D layers of C_{10}-BTBT crystals are more dominant on the a-alumina/KPI film. For the charge carrier transport, a 2D layer-by-layer crystal formation is more advantageous than a 3D crystal formation.[23] Improved 2D layer-by-layer crystal

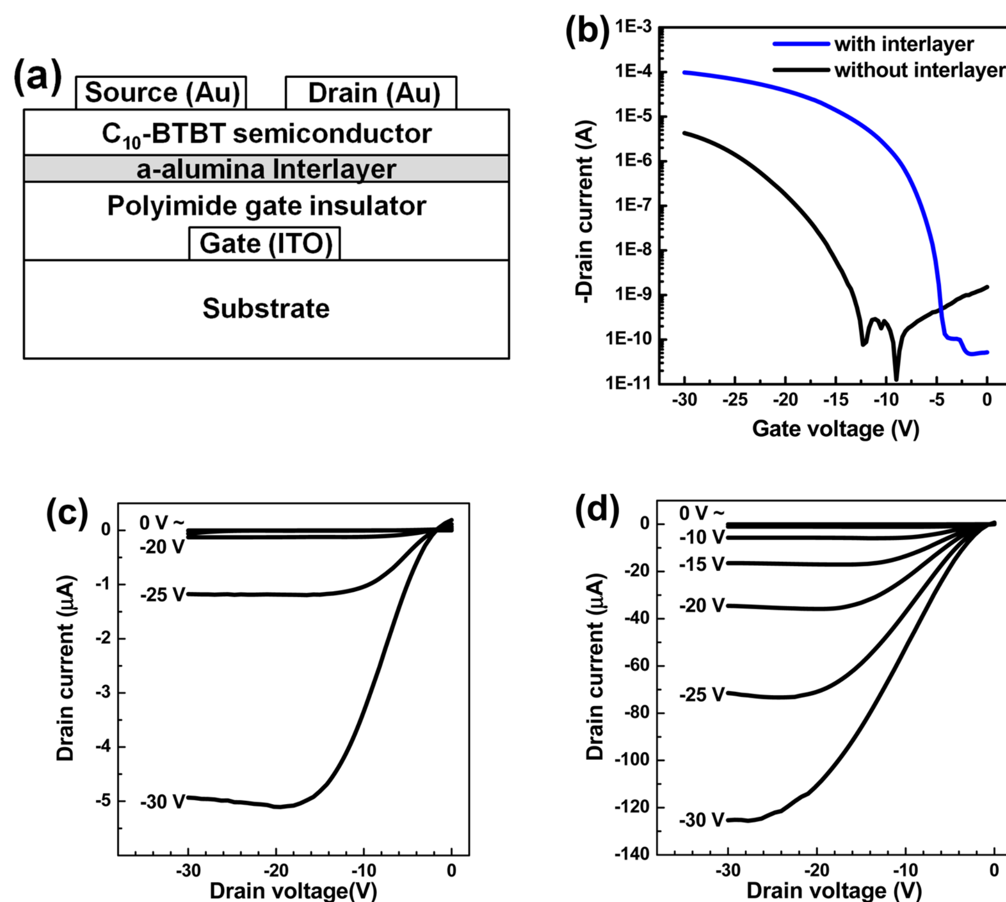

Figure 4. (a) Scheme of the OTFT device structure. (b) Transfer characteristics of the C_{10}-BTBT TFTs with and without the a-alumina interlayer. Output characteristics of the C_{10}-BTBT TFTs (c) with and (d) without the a-alumina interlayer.

Table 2. Electrical Characteristics of the C_{10}-BTBT TFTs with SiO_2, KPI, and a-Alumina/KPI Gate Insulators

gate insulator	mobility (average mobility[a]) [$cm^2/(V\ s)$]	V_{on} [V]	V_{th} [V]	*S*-slope [V/decade]	I_{on}/I_{off}
SiO_2	0.41 (0.39 ± 0.11)	−15.0	−21.9	2.46	6.33×10^5
KPI	0.18 (0.35 ± 0.15)	−12.3	−18.6	3.27	3.39×10^5
a-alumina/KPI	1.42 (1.35 ± 0.28)	−3.9	−7.0	0.42	2.05×10^6

[a]Average field-effect mobility of 10 TFT devices.

formation of the OSC by introduction of the a-alumina interlayer was also confirmed by XRD analysis. Figure 6a shows the out-of-plane XRD patterns of C_{10}-BTBT layers on the KPI and the a-alumina/KPI films. In the XRD patterns, there are (*00l*) reflections with an interlayer distance (*d*-spacing) of 3.32 and 3.41 nm, respectively, which correspond to the *c*-axis length of the single-crystal C_{10}-BTBT unit cell, 3.378 nm.[38] The dominant molecular arrangement of C_{10}-BTBT on KPI and a-alumina/KPI gate insulators are characterized by a 2D layer-by-layer structure along the *c*-axis direction. The (*001*) peak intensity of C_{10}-BTBT on a-alumina/KPI is 1.2 times higher than that of C_{10}-BTBT on bare KPI. The full width at half-maximum (fwhm) values were calculated from the rocking curves of the (*002*) reflections (Figure 6b). The fwhm values of the C_{10}-BTBT layers on KPI and a-alumina-KPI films were 0.99° and 0.79°, respectively. More broadening of the rocking

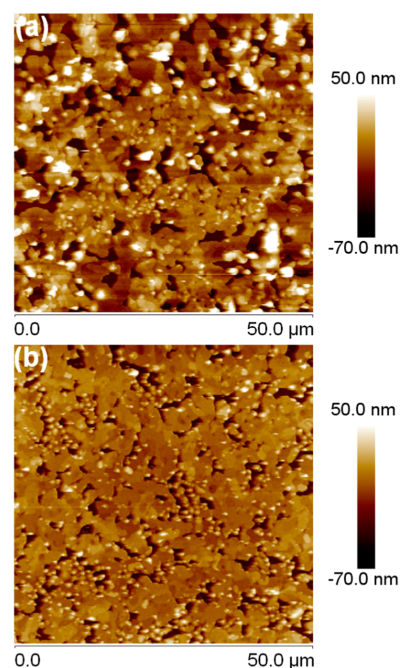

Figure 5. AFM images of C_{10}-BTBT layers on (a) KPI and (b) a-alumina/KPI films.

curve of the C_{10}-BTBT layers on the KPI gate insulator corresponds well to the AFM image, where much larger 3D islands of C_{10}-BTBT crystals were observed. By introducing the

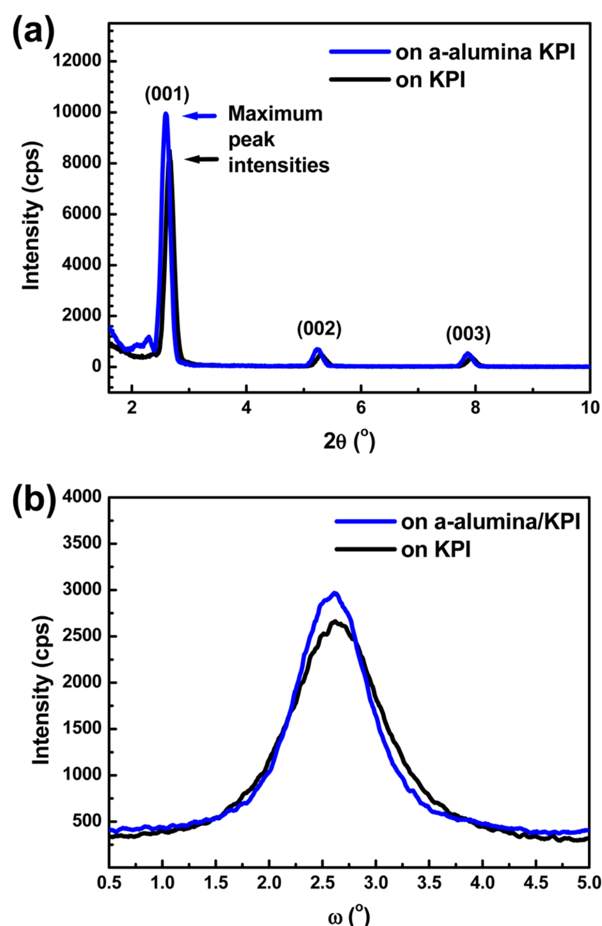

Figure 6. (a) XRD patterns and (b) rocking curves on the (*002*) reflections of C_{10}-BTBT layers on KPI and a-alumina/KPI films.

a-alumina interlayer, the crystal quality of the 2D-layered C_{10}-BTBT was improved. The surface properties of the gate insulators dramatically affect the OSC morphology in a bottom-gate OTFT. Effects of the surface properties on the morphologies of vacuum-evaporated OSCs with various OSC thicknesses have been widely studied. However, study on the morphologies of solution-processed OSCs is more limited, and more research efforts are needed to fully understand the OSC crystal formation at the interface.

According to the TGA results (Figures S1 and S2, Supporting Information), the organic residue should be included in the 200 °C-annealed interlayer due to the presence of an incompletely decomposed precursor. The existence of $NO_3{\cdot}(H_2O)_x$ was confirmed by the XPS analysis (Figure 1) and also by the nitrate antisymetric stretching mode (ν3, 1385 cm^{-1}) and the water bending mode (1728 cm^{-1}) of the infrared (IR) spectrum (labeled A and B, respectively, in Figure S8, Supporting Information).[39] The vertical composition profile of nitrate hydrate in the alumina layer was investigated by an Auger depth profile. As shown in Figure S9, Supporting Information, the nitrate-related functional moiety is present uniformly along the a-alumina interfacial layer. We confirmed that the remaining nitrate did not increase the leakage current density, as shown in Figure 3b.

The improved OTFT performance could be due to the additional generation of mobile charge carriers at the interface between the OSC and the gate insulator, as well as the enhanced crystal formation. According to the trap and release model, traps at the OSC/gate insulator interface capture field-effect carriers and V_{th} are strongly related to the voltage at which the trap states are occupied completely by field-effect carriers.[40−44] Recently, we reported that V_{th} of the C_{10}-BTBT TFTs could be shifted in a positive direction by doping the electron acceptor, such as 2,3,5,6-tetrafluoro-7,7,8,8-tetracyanoquinodimethane (F_4TCNQ), into the OSC layer.[20] With the doping, the charge transfer between the electron acceptor and the OSC occurred and more mobile holes appeared. Because of the increased number of mobile holes, the number of unoccupied trap states was reduced and the field-effect mobility increased.[43−46] In general, the oxide surface has a high density of charge traps which could capture field-effect carriers. However, at the OSC/a-alumina interface, electrons might be trapped selectively by the remaining nitrate, known as a strong electron acceptor, and more mobile holes could appear. The V_{th} shift in a positive direction and the increased field-effect mobility might be the result of a charge transfer between the remaining nitrate and C_{10}-BTBT.

Our results suggest that the introduction of the a-alumina interlayer could be a simple OGI-surface-treatment way to enhance OTFT performance by improving the crystal quality of OSC molecules and/or by formation of a charge transfer at the channel between the OSC and the interlayer. It is well-known that polyimide films could be fabricated by various continuous processes such as slot coating and blade coating processes. The polyimide and the a-alumina thin films in this study are expected to be applicable for a continuous in-line process.

■ CONCLUSION

In summary, we report a low-temperature-annealed sol−gel-derived a-alumnia interlayer between the OGI and the OSC for enhanced performance of OTFTs. To investigate the effect of the interlayer on OTFT performance, we fabricated solution-processed C_{10}-BTBT TFTs with the polyimide and the a-alumina/polyimide gate insulators. By introducing the interlayer, the field-effect mobility increased from 0.35 ± 0.15 to 1.35 ± 0.28 cm^2/V·s. Use of the a-alumina interlayer results in increasing the crystal quality of C_{10}-BTBT molecules. In addition, we believe that the remaining nitrate in the interlayer acts as an electron acceptor for increasing the number of mobile holes, resulting in the V_{th} shifting in a positive direction and the enhancement of field-effect mobility.

■ EXPERIMENTAL SECTION

For the synthesis of the poly(amic acid), the polyimide precursor, BPDA, and *p*-PDA were dissolved in *N*-methyl-2-pyrollidone (NMP). The solution was stirred until the solution viscosity reached the saturation point. The as-prepared poly(amic acid) solution with 5 wt % (weight percent to the poly(amic acid)) of DBU was spin-coated on patterned indium tin oxide (ITO)-coated glasses. The spin-coated films were annealed at 90 °C for 10 min and 200 °C for 40 min on a hot plate in ambient air. The final thickness of all the polyimide films was controlled to be 120 nm. The alumina interlayer was deposited on the polyimide gate insulator using a simple spin-coating method. Aluminum(III) nitrate nonahydrate ($Al(NO_3)_3{\cdot}9H_2O$) was dissolved in 2-butoxyethanol with a concentration of 7 wt %. The precursor solution was spin-coated at 2000 rpm for 30 s on the polyimide layer and annealed at 90 °C for 10 min and 200 °C for 40 min on a hot plate in ambient air.

Surface energies of the prepared films were calculated from contact angles of water and diiodomethane, which were measured by a PEONIX 300 contact angle analyzer. To predict surface energies of the

gate insulators, a geometric-mean approach by Owens and Wendt was applied.[47,48]

To determine the capacitance and insulating properties of the gate insulators, the MIM capacitor structures were prepared by deposition of the top gold electrode on the polyimide-coated ITO glass. The active area of the MIM devices was 50.24 mm^2. For electrical characterizations, we prepared bottom-gate, top-contact TFT devices. ITO-coated glass was used as the substrate, and the ITO was patterned (2 mm wide stripes) to produce the gate electrode. A 0.4 wt % solution of C_{10}-BTBT, synthesized by Svoboda's method,[49] in chloroform was spin-coated on the gate insulator layer at 3000 rpm for 30 s. After annealing at 80 °C for 30 min, 50 nm-thick source and drain gold electrodes were deposited by thermal evaporation on the semiconductor layer through a shadow mask, creating a transistor with a channel length (L) and a width (W) of 50 and 1000 μm, respectively.

■ ASSOCIATED CONTENT

Supporting Information

XRD pattern and IR spectrum of the alumina interlayer, transfer characteristics of organic thin-film transistors, and thermal gravimetric analysis curves of $Al(NO_3)_3 \cdot 9H_2O$. This information is available free of charge via the Internet at http://pubs.acs.org/.

■ AUTHOR INFORMATION

Corresponding Author

*E-mail: kjang@krict.re.kr (K.-S.J.); mhyi@krict.re.kr (M.H.Y.).

Notes

The authors declare no competing financial interest.

■ ACKNOWLEDGMENTS

This work was supported by a grant from the cooperative R&D program funded by the Korea Research Council for Industrial Science and Technology and was partially supported by the KRICT core project (KK-1302-C0, Development of Core Technology of Advanced Materials for Printing Processes) funded by the Ministry of Knowledge Economy.

■ REFERENCES

(1) Kelley, T. W.; Baude, P. F.; Gerlach, C.; Ender, D. E.; Muyres, D.; Haase, M. A.; Vogel, D. E.; Theiss, S. D. *Chem. Mater.* **2004**, *16*, 4413−4422.

(2) Chabinyc, M. L.; Salleo, A. *Chem. Mater.* **2004**, *16*, 4509−4521.

(3) Sokolov, A. N.; Roberts, M. E.; Bao, Z. *Mater. Today* **2009**, *12*, 12−20.

(4) Katz, H. E.; Huang, J. *Annu. Rev. Mater. Res.* **2009**, *39*, 71−92.

(5) Ortiz, R. P.; Facchetti, A.; Marks, T. J. *Chem. Rev.* **2010**, *110*, 205−239.

(6) Zhou, L.; Wanga, A.; Wu, S.-C.; Sun, J.; Park, S.; Jackson, T. N. *Appl. Phys. Lett.* **2006**, *88*, 083502.

(7) Gelinck, G. H.; Huitema, H. E. A.; van Veenedaal, E.; Cantatore, E.; Schrijnemakers, L.; van der Putten, J. B. P. H.; Geuns, T. C. T.; Beenhakkers, M.; Giesbers, J. B.; Huisman, B.-H.; Meijer, E. J.; Benito, E. M.; Touwslager, F. J.; Marsman, A. W.; van Rens, B. J. E.; de Leeuw, D. M. *Nat. Mater.* **2004**, *3*, 106−110.

(8) Someya, T.; Kato, Y.; Sekitani, T.; Iba, S.; Noguchi, Y.; Murase, Y.; Kawaguchi, H.; Sakurai, T. *Proc. Natl. Acad. Sci. U.S.A.* **2005**, *102*, 12321−12325.

(9) Baude, P. F.; Ender, D. A.; Haase, M. A.; Kelley, T. W.; Muyres, D. V.; Theiss, S. D. *Appl. Phys. Lett.* **2003**, *82*, 3964−3966.

(10) Klauk, H.; Zschieschang, U.; Pflaum, J.; Halik, M. *Nature* **2007**, *445*, 745−748.

(11) Ebata, H.; Izawa, T.; Miyazaki, E.; Takimiya, K.; Ikeda, M.; Kuwabara, H.; Yui, T. *J. Am. Chem. Soc.* **2007**, *129*, 15732−15733.

(12) Takimiya, K.; Yamamoto, T.; Ebata, H.; Izawa, T. *Sci. Technol. Adv. Mater.* **2007**, *8*, 273−276.

(13) Takimiya, K.; Shinamura, S.; Osaka, I.; Miyazaki, E. *Adv. Mater.* **2011**, *23*, 4347−4370.

(14) Liu, C.; Minari, T.; Lu, X.; Kumatani, A.; Takimiya, K.; Tsukagoshi, K. *Adv. Mater.* **2011**, *23*, 523−526.

(15) Minemawari, H.; Yamada, T.; Matsui, H.; Tsutsumi, J.; Haas, S.; Chiba, R.; Kumai, R.; Hasegawa, T. *Nature* **2011**, *475*, 364−367.

(16) Uemura, T.; Hirose, Y.; Uno, M.; Takimiya, K.; Takeya, J. *Appl. Phys. Express* **2009**, *2*, 111501−111503.

(17) Soeda, J.; Hirose, Y.; Yamagishi, M.; Nakao, A.; Uemura, T.; Nakayama, K.; Uno, M.; Nakazawa, Y.; Takimiya, K.; Takeya, J. *Adv. Mater.* **2011**, *23*, 3309−3314.

(18) Kano, M.; Minari, T.; Tsukagoshi, K. *Appl. Phys. Lett.* **2009**, *94*, 143304.

(19) Endo, T.; Nagase, T.; Kobayashi, T.; Takimiya, K.; Ikeda, M.; Naito, H. *Appl. Phys. Express* **2010**, *3*, 121601.

(20) Jang, K.-S.; Kim, W. S.; Won, J.-M.; Kim, Y.-H.; Myung, S.; Ka, J.-W.; Kim, J.; Ahn, T.; Yi, M. H. *Phys. Chem. Chem. Phys.* **2013**, *15*, 950−956.

(21) Fontaine, P.; Goguenheim, D.; Deresmes, D.; Vuillaume, D.; Garet, M.; Rondelez, F. *Appl. Phys. Lett.* **1993**, *62*, 2256−2258.

(22) Li, L.; Tang, Q.; Li, H.; Hu, W. *J. Phys. Chem. B* **2008**, *112*, 10405−10410.

(23) Shao, W.; Dong, H.; Jiang, L.; Hu, W. *Chem. Sci.* **2011**, *2*, 590−600.

(24) McCulloch, I.; Heeney, M.; Bailey, C.; Genevicius, K.; Macdonald, I.; Shkunov, M.; Sparrowe, D.; Tierney, S.; Wagner, R.; Zhang, W.; Chabinyc, M. L.; Kline, R. J.; McGehee, M. D.; Toney, M. F. *Nat. Mater.* **2006**, *5*, 328−333.

(25) Li, Y.; Singh, S. P.; Sonar, P. *Adv. Mater.* **2010**, *22*, 4862−4866.

(26) Li, Y.; Sonar, P.; Singh, S. P.; Soh, M. S.; van Meurs, M.; Tan, J. *J. Am. Chem. Soc.* **2011**, *133*, 2198−2204.

(27) Giri, G.; Verploegen, E.; Mannsfeld, S. C. B.; Atahan-Evrenk, S.; Kim, D. H.; Lee, S. Y.; Becerril, H. A.; Aspuru-Guzik, A.; Toney, M. F.; Bao, Z. *Nature* **2011**, *480*, 504−508.

(28) Walter, S. R.; Youn, J.; Emery, J. D.; Kewalramani, S.; Hennek, J. W.; Bedzyk, M. J.; Facchetti, A.; Marks, T. J.; Geiger, M. *J. Am. Chem. Soc.* **2012**, *134*, 11726−11733.

(29) Chen, H.; Guo, Y.; Yu, G.; Zhao, Y.; Zhang, J.; Gao, D.; Liu, H.; Liu, Y. *Adv. Mater.* **2012**, *24*, 4618−4622.

(30) Li, J.; Zhao, Y.; Tan, H. S.; Guo, Y.; Di, C.-A.; Yu, G.; Liu, Y.; Lin, M.; Lim, S. H.; Zhou, Y.; Su, H.; Ong, B. S. *Sci. Rep.* **2012**, *2*, 585.

(31) Kang, I.; An, T. K.; Hong, J.-a.; Yun, H.-J.; Kim, Y. R.; Chung, D. S.; Park, C. E.; Kim, Y.-H.; Kwon, S.-K. *Adv. Mater.* **2013**, *25*, 524−528.

(32) Kim, M.-G.; Kanatzidis, M. G.; Facchetti, A.; Marks, T. J. *Nat. Mater.* **2011**, *10*, 382−388.

(33) Ahn, T.; Choi, Y.; Jung, H. M.; Yi, M. *Org. Electron.* **2009**, *10*, 12−17.

(34) Chou, C.-H.; Kwan, W. L.; Hong, Z.; Chen, L.-M.; Yang, Y. *Adv. Mater.* **2011**, *23*, 1282−1286.

(35) Sun, Y.; Seo, J. H.; Takacs, C. J.; Seifter, J.; Heeger, A. J. *Adv. Mater.* **2011**, *23*, 1679−1683.

(36) Jia, Q. X.; Chang, L. H.; Anderson, W. A. *Thin Solid Films* **1995**, *259*, 264−269.

(37) Lee, J.-S.; Joo, S.-K. *Appl. Phys. Lett.* **2002**, *30*, 2602−2604.

(38) Izawa, T.; Miyazaki, E.; Takimiya, K. *Adv. Mater.* **2008**, *20*, 3388−3392.

(39) Goebbert, D. J.; Garand, E.; Wende, T.; Bergmann, R.; Meijer, G.; Asmis, K. R.; Neumark, D. M. *J. Phys. Chem. A* **2009**, *113*, 7584−7592.

(40) Ma, L.; Lee, W. H.; Park, Y. D.; Kim, J. S.; Lee, H. S.; Cho, K. *Phys. Rev. Lett.* **2004**, *92*, 1116802.

(41) Jaiswal, M.; Menon, R. *Polym. Int.* **2006**, *55*, 1371−1384.

(42) Abe, Y.; Hasegawa, T.; Takahashi, Y.; Yamada, T.; Tokura, Y. *Appl. Phys. Lett.* **2005**, *87*, 153506.

(43) Horowitz, G.; Delannoy, P. *J. Appl. Phys.* **1991**, *70*, 469−475.

(44) Lim, E.; Jung, B.-J.; Chikamatsu, M.; Azumi, R.; Yoshida, Y.; Yase, K.; Do, L.-M.; Shim, H.-K. *J. Mater. Chem.* **2007**, *17*, 1416−1420.

(45) Kobayashi, S.; Nishikawa, T.; Takenobu, T.; Mori, S.; Shimoda, T.; Mitani, T.; Shimotani, H.; Yoshimoto, N.; Ogawa, S.; Iwasa, Y. *Nat. Mater.* **2004**, *3*, 317−322.
(46) Possanner, S. K.; Zojer, K.; Pacher, P.; Zojer, E.; Schürrer, F. *Adv. Funct. Mater.* **2009**, *19*, 958−967.
(47) Owens, D. K.; Wendt, R. C. *J. Appl. Polym. Sci.* **1969**, *13*, 1741−1747.
(48) Huang, X. D.; Bhangale, S. M.; Moran, P. M.; Yakovlev, N. L.; Pan, J. *Polym. Int.* **2003**, *52*, 1064−1069.
(49) Košata, B.; Kozmik, V.; Svoboda, J.; Novotná, V.; Vanêk, P.; Glogarová, M. *Liq. Cryst.* **2003**, *30*, 603−610.